An h-adaptive spacetime-discontinuous Galerkin method for linear elastodynamics

Reza Abedi[*] — Robert B. Haber[*] — Shripad Thite[, ***]**
Jeff Erickson[**]

[*] *Department of Theoretical & Applied Mechanics* ([**] *Computer Science*)
University of Illinois at Urbana-Champaign
104 South Wright St., Urbana, IL 61801 USA

{rabedi, r-haber, jeffe}@uiuc.edu; sthite@win.tue.nl

[***] *Currently, Department of Mathematics and Computer Science, Technische Universiteit Eindhoven, Postbus 513, 5600 MB, Eindhoven, The Netherlands*

ABSTRACT. *We present an h-adaptive version of the spacetime-discontinuous Galerkin (SDG) finite element method for linearized elastodynamics (Abedi* et al.*, 2006). The adaptive version inherits key properties of the basic SDG formulation, including element-wise balance of linear and angular momentum, complexity that is linear in the number of elements and oscillation-free shock capturing. Unstructured spacetime grids allow simultaneous adaptation in space and time. A localized patch-by-patch solution process limits the cost of reanalysis when the error indicator calls for more refinement. Numerical examples demonstrate the method's performance and shock-capturing capabilities.*

RÉSUMÉ. *Nous présentons une version h-adaptative de la méthode de Galerkin discontinu espace temps (SDG) pour l'élastodynamique linéaire (Abedi* et al.*, 2006). La version adaptative hérite des principales propriétés de la formulation de base de la méthode SDG, comme par exemple l'équilibre par élément de la quantité de mouvement et du moment cinétique, la complexité informatique linéairement proportionnelle au nombre d'éléments et la capture sans oscillation de chocs. Les maillages, qui sont non structurés en espace temps, permettent l'adaptation simultanée en espace et en temps. Une procédure de résolution localisée par patch permet de limiter le coût de la réanalyse après le raffinement local imposé par l'indicateur d'erreur. Des exemples numériques sont présentés et montrent l'efficacité de la méthode et plus particulièrement sa capacité à capter des chocs.*

KEYWORDS: *adaptive analysis, discontinuous Galerkin, spacetime, elastodynamics, shocks.*

MOTS-CLÉS : *analyse adaptative, Galerkin discontinu, espace temps, élastodynamique, chocs.*

REMN – 15/2006. Space or/and time adaptive strategies, pages 619 to 642

1. Introduction

Simulations of elastodynamic wave propagation often involve multi-scale analysis problems that require adaptive computational procedures. Shocks and sharp wavefronts introduce length and time scales that are typically far smaller than the smallest features of the macroscopic analysis domain. Direct simulation of material microstructure and other small-scale geometric features can similarly introduce a multi-scale character to the problem. In other problems, crack-tip singular fields or fracture process zones are the source of small-scale solution features. In all these cases, numerical methods based on uniform mesh refinement can lead to intractable problem sizes. Graded meshes generated by adaptive refinement procedures are a practical response that ensures accurate solutions at a reasonable cost.

Multi-scale problems sometimes involve moving small-scale features (e.g., propagating cracks or sharp wavefronts) whose trajectories are hard to predict *a priori*. In such cases, static mesh refinement is inadequate, and adaptive procedures are the only available methods that are capable of capturing the fine-scale physics. Ideally, the solution procedure should be adaptive in both space and time, since Courant limits can impose unacceptable restrictions on the global time-step size in methods that are adaptive in space only. Not only does this increase the computational load, but it can also cause excessive numerical dispersion (Becache *et al.*, 2005). Beyond the requirements for adaptive modeling, the underlying numerical method must be computationally efficient and capable of resolving shocks and other small-scale features without spurious oscillations or excessive numerical dissipation.

This paper proposes an h-adaptive version of the spacetime-discontinuous Galerkin (SDG) finite element method for elastodynamic analysis (Abedi *et al.*, 2006) to address the above requirements. We give brief reviews of existing adaptive algorithms and of discontinuous Galerkin methods for elastodynamics before introducing the new method.

1.1. *Conforming adaptive analysis methods for elastodynamics*

While there exists an extensive literature on adaptive analysis methods for elastostatics (Guo *et al.*, 1986a; Guo *et al.*, 1986b; Mackerle, 2001), the literature on adaptive schemes for elastodynamics is more limited. Cho and Youn (Cho *et al.*, 1995) propose a scheme based on spacetime interpolations that is hierarchical p-adaptive in time. The spatial discretization and the global time-step size are fixed and non-adaptive. The temporal polynomial order is determined adaptively, but is uniform over the space mesh within each time step. Safjan and Oden (Safjan *et al.*, 1993) present a semi-discrete scheme that is hp-adaptive in space only; the time-step size and temporal integration scheme are not controlled adaptively. (Wiberg *et al.*, 1992) propose two adaptive schemes that are both hp-adaptive in space. One is a semi-discrete method based on Newmark integration that is h-adaptive in time; the other is a conforming spacetime method using Cartesian-product basis functions that is p-adaptive in

time on a per-element basis. Adaptive multi-grid solvers applied to frequency-domain methods are proposed in (Joo *et al.*, 1988; Han *et al.*, 2002). (Bajer, 1989; Bajer *et al.*, 1991) use conforming, non-prismatic, spacetime elements to implement a purely r-adaptive procedure with a spatially uniform time step. Nodes migrate in space to minimize error subject to a fixed mesh connectivity; there is no temporal adaptivity in this method.

1.2. *Discontinuous Galerkin methods for elastodynamics*

Conforming finite element methods tend to generate spurious high-frequency oscillations when shocks are present unless the solution is stabilized, for example, by filtering or numerical damping. Unfortunately, stabilization causes numerical dissipation that limits the accuracy of these methods. The balance properties of conforming methods tend to be global in nature, while multi-scale problems demand balance over local subdomains to ensure accurate resolution of the fine-scale response. Discontinuous Galerkin methods have received increasing attention in recent years due to their ability to generate oscillation-free solutions without the introduction of extraneous stabilization. Fully discontinuous methods also offer element-wise balance properties that are attractive for multi-scale analysis.

Time-discontinuous Galerkin methods, first introduced in (Reed *et al.*, 1973; Lesaint *et al.*, 1974), feature spacetime basis functions that are continuous in space and discontinuous across a series of constant-time manifolds. The collection of elements filling the spacetime volume between two adjacent constant-time manifolds is called a *slab*. The solution is assumed to be continuous within a slab, and weak enforcement of various jump conditions in the variational formulation approximates the appropriate level of continuity between slabs. Hulbert and Hughes introduced a time-discontinuous Galerkin method for elastodynamics in (Hughes *et al.*, 1988; Hulbert *et al.*, 1990). The stability and convergence properties of time-discontinuous Galerkin methods are analyzed in (French, 1993; Johnson, 1993; Costanzo *et al.*, 2005).

(Li *et al.*, 1996, 1998, Wiberg *et al.*, 1999) implement h-adaptive procedures for elastodynamics using the time-discontinuous Galerkin method. The arrangement of spacetime elements within each slab allows for simultaneous mesh adaptation in space and time. The discontinuous basis admits spacetime meshes that are nonconforming across inter-slab boundaries, and this facilitates adaptive refinement and coarsening between slabs. However, the continuous basis within each slab requires a new computation for the entire slab whenever any element in the slab is refined. This increases the overhead associated with adaptive refinement. The slab-wise continuous basis leads to balance properties at the level of complete slabs, a scale that is larger than desired in the context of multi-scale analysis.

Spacetime-discontinuous Galerkin (SDG) finite element methods were first introduced by Richter for the wave equation (Richter, 1994). SDG methods use spacetime Galerkin bases that admit discontinuities across all inter-element boundaries in the

spacetime mesh. It is not necessary to organize elements into slabs; fully unstructured nonconforming spacetime grids are admissible, so it is natural (although not mandatory) to abandon the notion of a global time step and instead determine the time interval locally for individual spacetime elements. (Yin *et al.*, 2000; Yin, 2002) propose the first SDG method for linear elastodynamics ; an improved formulation is proposed in (Abedi *et al.*, 2006) that provides the basis for the adaptive algorithm introduced in this paper. The latter formulation guarantees balance of linear and angular momentum to within machine precision on every spacetime element; a desirable property for multi-scale applications. Here balance is defined with respect to physically and mathematically consistent Godunov values, rather than numerical fluxes.

SDG methods have the same oscillation-free property as time-discontinuous methods, but with better shock-capturing capabilities. If the spacetime mesh is constructed to satisfy a *causality constraint*, then a direct patch-by-patch advancing-front solution procedure is possible, with linear computational complexity in the number of patches (cf. Section 3.1). For causal meshes, the solution on any given patch is independent of all subsequent patches in the solution sequence. Thus, a refinement operation requires the solution on only a single patch to be discarded, a property that substantially reduces the cost of adaptive algorithms. The SDG method fully supports nonconforming spacetime grids, and this facilitates the construction of heavily graded meshes in our adaptive procedure. The discontinuous formulation has intrinsic support for jumps in the mechanical fields, so there is no need to implement data projections when the mesh is refined or coarsened.

We use an extended version of the *Tent Pitcher* algorithm (Üngör *et al.*, 2002; Erickson *et al.*, 2002) to construct causal spacetime meshes that adapt simultaneously in space and time. While our method balances linear and angular momentum on every spacetime element, the method is dissipative with respect to energy balance. Hence, the goal of our adaptive scheme is to limit the numerical energy dissipation and to distribute it evenly over the spacetime mesh. In order to meet this objective, we use an error indicator based on the element-wise dissipation to drive adaptive refinement and coarsening.

1.3. *Scope of this paper*

The remainder of this paper is organized as follows. Section 2 summarizes a spacetime formulation for continuum elastodynamics in the framework of differential forms and the exterior calculus (Abedi *et al.*, 2006) and formulates the corresponding discontinuous Galerkin finite element method. We describe our adaptive implementation in Section 3, including an advancing-front spacetime meshing algorithm (Erickson *et al.*, 2002; Abedi *et al.*, 2004) with extensions for local grid refinement and coarsening and an error indicator that controls the element-wise numerical dissipation. A crack-tip wave scattering example, including numerical convergence studies and a comparison between adaptive and non-adaptive algorithms, is presented in Section 4, followed by concluding remarks in Section 5.

2. Formulation

2.1. *Spacetime manifolds and notation for differential forms*

We use differential forms and the exterior calculus on manifolds to develop a spacetime continuum theory for linearized elastodynamics. Let d be the spatial dimension, and let the reference spacetime analysis domain D be an open $(d+1)$-manifold in $\mathbb{E}^d \times \mathbb{R}$ with a regular boundary. The spacetime coordinates $\left(x^1, \ldots, x^d, t\right)$ are the material coordinates associated with the undeformed configuration followed by the time coordinate and are defined with respect to the ordered basis $(\mathbf{e}_1, \ldots, \mathbf{e}_d, \mathbf{e}_t)$. The dual basis is $\left(\mathbf{e}^1, \ldots, \mathbf{e}^d, \mathbf{e}^t\right)$. We follow the standard summation convention; latin indices range from 1 through d, except the index 't' which denotes time and does not imply summation when repeated.

The standard basis for top forms on D is $\mathbf{\Omega} = \mathbf{d}x^1 \wedge \ldots \wedge \mathbf{d}x^d \wedge \mathbf{d}t$, and the d-form $\mathbf{d}\hat{x}_j$ is defined by: $\mathbf{d}x^j \wedge \mathbf{d}\hat{x}_k = \delta^j_{\ k}\mathbf{\Omega}; \mathbf{d}t \wedge \mathbf{d}\hat{x}_k = \mathbf{0}$. We define the *temporal insertion* as $\mathbf{i} := \mathbf{i}_{\bar{\mathbf{e}}_t}$, in which $\bar{\mathbf{e}}_t$ is a vector field on D with uniform value $\mathbf{e}_t$. Thus, $\mathbf{d}t \wedge \mathbf{i}\mathbf{\Omega} = \mathbf{\Omega}$ and $\mathbf{d}x^j \wedge \mathbf{i}\mathbf{\Omega} = \mathbf{0}$. We use forms with both vector and scalar coefficients to develop the theory; the exterior (wedge) product of two vector-valued forms is the form with scalar coefficients defined by:

$$(\mathbf{a} \otimes \psi) \wedge (\mathbf{b} \otimes \omega) = (\mathbf{a} \cdot \mathbf{b})\, \psi \wedge \omega \qquad [1]$$

in which $\mathbf{a}, \mathbf{b} \in \mathbb{E}^d(D)$ are vector fields and ψ, ω are forms on D. See (Bishop *et al.*, 1980; Fleming, 1964; Spivak, 1965) for more complete expositions of differential forms and tensor calculus on manifolds.

2.2. *Mechanical fields*

Let the ordered set $\{Q_\alpha\}$ be a partition of the spacetime domain D into open subdomains with regular boundaries. We define a broken Sobolev space over $\{Q_\alpha\}$ as $V(D) := \{\mathbf{w} \in L^2(D) : \mathbf{w}|_{Q_\alpha} \in H^2(Q_\alpha)\}$. Note that $V(D)$ admits discontinuities across the boundaries between adjacent subdomains. For any $Q \in \{Q_\alpha\}$, let $V^Q := V(D)|_Q = H^2(Q)$.

Let $\mathbf{u} \in V$ denote the *displacement field on* D, where $\mathbf{u} = u_i \mathbf{e}^i$. The *velocity* is the 1-form with vector coefficients given by $\mathbf{v} := \dot{\mathbf{u}} \otimes \mathbf{d}t = \dot{u}_i \mathbf{e}^i \otimes \mathbf{d}t$, and the *linearized strain* is given by $\mathbf{E} = E_{ij}\mathbf{e}^i \otimes \mathbf{d}x^j$, where $E_{ij} := \frac{1}{2}(u_{i,j} + u_{j,i})$. The *strain-velocity* is the 1-form defined by $\varepsilon := \mathbf{E} + \mathbf{v}$.

The force-like fields are d-forms on D with vector coefficients. We introduce the *stress*:

$$\sigma = \sigma^{ij}\mathbf{e}_i \otimes \mathbf{d}\hat{\mathbf{x}}_j, \qquad [2]$$

where σ^{ij} are the components of stress tensor. The restriction of the stress to any spacetime d-manifold $\Gamma \subset \overline{D}$ delivers the *surface traction* on Γ. The *linear momentum density* is defined as:

$$\mathbf{p} = p^i \mathbf{e}_i \otimes \mathbf{i\Omega}. \qquad [3]$$

in which the vector field $\overline{\mathbf{p}} = (p^1, \cdots, p^d) : D \to \mathbb{E}^d$ is the linear momentum measured per unit volume in the reference configuration. These combine to form the spacetime linear momentum flux:

$$\mathbf{M} = \boldsymbol{\sigma} - \mathbf{p}. \qquad [4]$$

The *body force density* is given by:

$$\mathbf{b} = b^i \mathbf{e}_i \otimes \mathbf{\Omega}. \qquad [5]$$

where $\bar{\mathbf{b}} = (b^1, \cdots, b^d) : D \to \mathbb{E}^d$ is the vector field that delivers body force per unit mass on D.

The *total energy density* $\mathbf{\Phi} = \Phi\mathbf{\Omega}$ is the non-negative $(d+1)$-form with scalar coefficient such that $\Phi = K + U$, in which K and U are the *kinetic energy density* and the *internal energy density* respectively, each measured per unit volume in the undeformed configuration. The form of the function Φ for the case of linear elastodynamic response is given in Subsection 2.5.

2.3. *Kinematic compatibility*

Kinematic compatibility requires the limiting displacement values, $\mathbf{u}^+$ and $\mathbf{u}^-$, on opposing sides of any spacetime d-manifold $\Gamma \subset \overline{D}$ to match. That is:

$$(\mathbf{u}^+ - \mathbf{u}^-)|_\Gamma = \mathbf{0}. \qquad [6]$$

In lieu of [6], we enforce an equivalent system of boundary jump conditions (Petracovici, 2004) on all subdomains $Q \subset D$:

$$(\varepsilon^* - \varepsilon)\,|_{\partial Q} = \mathbf{0} \qquad [7a]$$

$$(\mathbf{u}_0^* - \mathbf{u}_0)\,|_{\partial Q} = \mathbf{0} \qquad [7b]$$

in which a superscript "*" denotes a physically consistent target value that is uniquely defined on any d-manifold embedded in $\overline{D}$ by causality, by prescribed boundary or initial data, or by the solution to a local Riemann problem (Abedi *et al.*, 2006).

A subscript "0" indicates a local projection of the displacement field onto a zero-energy subspace characterized by vanishing velocity and strain. Specific definitions of the target values appear in 2.6.

2.4. *Momentum and energy balance*

Balance of linear momentum requires that:

$$\int_{\partial Q} \mathbf{M} + \int_{Q} \rho \mathbf{b} = 0 \quad \forall Q \subset D \tag{8}$$

in which ρ is the mass density per unit volume in the reference configuration. Equation [8] also implies balance of angular momentum when the stress tensor σ is symmetric (Abedi *et al.*, 2006).

The following system enforces [8] *via* the Stokes Theorem while accounting for possible jumps in $\mathbf{M}$. It also enforces compatibility with a target momentum flux $\mathbf{M}^*$ that is defined uniquely on every d-manifold embedded in $\overline{D}$ (see 2.6). For all $Q \subset D$,

$$(\mathbf{dM} + \rho \mathbf{b})|_{Q \setminus \Gamma^{\mathrm{J}}} = \mathbf{0} \tag{9a}$$

$$(\mathbf{M}^* - \mathbf{M})|_{\partial Q \cup (Q \cap \Gamma^{\mathrm{J}})} = \mathbf{0} \tag{9b}$$

where Γ^{J} is the jump set of $\mathbf{M}$.The component form of [9a] is $\left[\sigma^{ij}{}_{,j} + \rho(b^i - \ddot{u}^i)\right] e_i \otimes \mathbf{\Omega} = \mathbf{0}$ on $Q \setminus \Gamma^{\mathrm{J}}$which is the familiar Equation of Motion.

Energy balance requires:

$$\int_{\partial Q} \mathbf{N} + \int_{Q} \dot{\mathbf{u}} \wedge \rho \mathbf{b} = 0 \quad \forall Q \subset D, \tag{10}$$

where $\mathbf{N} := -\mathbf{i}\mathbf{\Phi} + \dot{\mathbf{u}} \wedge \sigma$ is the *spacetime flux of total energy*.

2.5. *Constitutive model*

We restrict our attention to materials with linear elastodynamic response. That is, we assume there exists a spacetime total energy density field of the form:

$$\mathbf{\Phi}(\varepsilon) = \frac{1}{2} \varepsilon \wedge \mathbf{C}\varepsilon = \frac{1}{2} \left(E_{ij} C^{ijkl} E_{kl} + \rho \dot{u}_i \delta^{ij} \dot{u}_j \right) \mathbf{\Omega}, \tag{11}$$

where $\mathbf{C}$ is a linear transformation of 1-forms into d-forms such that:

$$\sigma + \mathbf{p} = \frac{\partial \mathbf{\Phi}}{\partial \varepsilon} \Rightarrow \qquad \sigma + \mathbf{p} = \mathbf{C}\varepsilon \qquad [12a]$$

$$\sigma = \frac{\partial \mathbf{\Phi}}{\partial \mathbf{E}} \Rightarrow \quad \sigma = \mathbf{C}\mathbf{E} \quad \text{or } \sigma^{ij} = C^{ijkl}E_{kl} \qquad [12b]$$

$$\mathbf{p} = \frac{\partial \mathbf{\Phi}}{\partial \mathbf{v}} \Rightarrow \qquad \mathbf{p} = \mathbf{C}\mathbf{v} \quad \text{or } p^i = \rho\delta^{ij}\dot{u}_j. \qquad [12c]$$

Here δ^{ij} is the Kronecker delta and the components C^{ijkl} of the positive-definite elasticity tensor exhibit the usual major and minor symmetries - a structure that ensures symmetry of σ. The momentum flux is related to the strain-velocity *via* the linear transformation:

$$\mathbf{M} = \hat{\mathbf{C}}\varepsilon := \mathbf{C}(\mathbf{E} - \mathbf{v}), \qquad [13]$$

and the spacetime flux of total energy for linear elastodynamic response reduces to:

$$\mathbf{N} = \frac{1}{2}\left(\dot{\mathbf{u}} \wedge \mathbf{M} + \varepsilon \wedge \mathbf{i}\sigma\right). \qquad [14]$$

2.6. *Boundary/initial conditions*

Consider a subdomain $Q \subset D$. The target values $\mathbf{u}_0^*$, ε^* and $\mathbf{M}^*$ in [7] and [9b] provide a unified mechanism for enforcing boundary conditions consistent with prescribed boundary and initial data on $\partial Q \cap \partial D$ or with causality on $\partial Q \setminus \partial D$. We use undecorated symbols and symbols decorated with a superscript "$+$" to denote, respectively, the interior and exterior traces of a quantity on ∂Q. A superscript "G" indicates a *Godunov value* on ∂Q that solves a local Riemann problem, as described in (Abedi *et al.*, 2006). An underlined symbol denotes prescribed initial or boundary data on ∂D. Next, we introduce two partitions of ∂Q that determine how the target values are computed.

The *temporal partition* is used to determine the target values $\mathbf{u}_0^*$ on ∂Q (see Figure 1a). The *temporal inflow boundary of* Q, denoted by ∂Q^{ti}, consists of all points $\mathbf{x} \in \partial Q$ where the temporal basis vector $\mathbf{e}_t$ points inward relative to Q. The *temporal outflow boundary of* Q is $\partial Q^{\mathrm{to}} := \partial Q \setminus \partial Q^{\mathrm{ti}}$.

The *causal partition* of ∂Q is used to determine the target values for ε^* and $\mathbf{M}^*$ based on prescribed initial/boundary data or on the characteristics associated with elastic wave propagation (see Figure 1b). We say that a spacetime d-manifold is *causal* if and only if it has a zero intersection with the union of the dynamic domains of influence of all its points. This implies that, everywhere on a causal subdomain of

∂Q, the characteristic directions are either all outward or all inward relative to Q. We partition ∂Q into its causal and noncausal parts, $\partial Q^{\rm c}$ and $\partial Q^{\rm nc}$, and we further partition $\partial Q^{\rm c}$ into a *causal inflow* part $\partial Q^{\rm ci}$ and a *causal outflow* part $\partial Q^{\rm co}$ according to whether the local characteristic directions are all inward or all outward relative to Q. In this work, we restrict our attention to *material* noncausal surfaces that are everywhere tangent to $\mathbf{e}_t$.

We also assume a disjoint partition of the noncausal boundary into two regions where either $\mathbf{M}$ or ε is prescribed: $\partial D^{\rm nc} = \partial D^{\mathbf{M}} \cup \partial D^{\varepsilon}$.

The target values provide a unified means for specifying jump, boundary and initial conditions based on the temporal and causal partitions. For every $Q \subset D$, the target values are given by:

$$\mathbf{u}_0^*|_{\partial Q} = \begin{cases} \mathbf{u}_0 & \text{on } \partial Q^{\rm to} \\ \mathbf{u}_0^+ & \text{on } \partial Q^{\rm ti} \setminus \partial D^{\rm ti} \\ \underline{\mathbf{u}}_0 & \text{on } \partial Q^{\rm ti} \cap \partial D^{\rm ti} \end{cases} \quad [15a]$$

$$\mathbf{M}^* = \begin{cases} \mathbf{M} & \text{on } \partial Q^{\rm co} \cup (\partial Q \cap \partial D^{\varepsilon}) \\ \mathbf{M}^+ & \text{on } \partial Q^{\rm ci} \setminus \partial D^{\rm ci} \\ \mathbf{M}^{\rm G}(\mathbf{M}, \mathbf{M}^+, \mathbf{a}_{\partial Q}) & \text{on } \partial Q^{\rm nc} \setminus \partial D^{\rm nc} \\ \underline{\mathbf{M}} & \text{on } \partial Q \cap \left(\partial D^{\rm ci} \cup \partial D^{\mathbf{M}}\right) \end{cases} \quad [15b]$$

$$\varepsilon^* = \begin{cases} \varepsilon & \text{on } \partial Q^{\rm co} \cup \left(\partial Q \cap \partial D^{\mathbf{M}}\right) \\ \varepsilon^+ & \text{on } \partial Q^{\rm ci} \setminus \partial D^{\rm ci} \\ \varepsilon^{\rm G}(\varepsilon, \varepsilon^+, \mathbf{a}_{\partial Q}) & \text{on } \partial Q^{\rm nc} \setminus \partial D^{\rm nc} \\ \underline{\varepsilon} & \text{on } \partial Q \cap \left(\partial D^{\rm ci} \cup \partial D^{\varepsilon}\right) \end{cases} \quad [15c]$$

The Godunov values derive from solutions to local Riemann problems (closed-form expressions are provided in (Abedi *et al.*, 2006)). They provide physically and mathematically consistent target values on $\partial Q^{\rm nc} \setminus \partial D^{\rm nc}$ that hold whether or not a shock is present.

2.7. *Discrete formulation*

We obtain a discontinuous Galerkin finite element method by associating the partition $\{Q_\alpha\}$ with a spacetime finite element mesh and by considering a finite-dimensional subspace of V, $V_h := \left\{\mathbf{w} \in V : \mathbf{w}|_{Q_\alpha} \in V_h^{Q_\alpha}\right\}$, in which $V_h^{Q_\alpha}$ is a finite-dimensional subspace of $H^2(Q_\alpha)$. We use spacetime simplex elements and polynomial spaces, $V_h^{Q_\alpha} = \mathbf{P}^n(Q_\alpha)$, where $\mathbf{P}^n(Q_\alpha)$ is the space of vector fields on Q_α whose components are complete polynomials of order n.[1] The discrete weighted

1. The polynomial order n must satisfy $n \geq 1$ for $d = 1$ and $n \geq 2$ for $d = 2, 3$ (Abedi *et al.*, 2006).

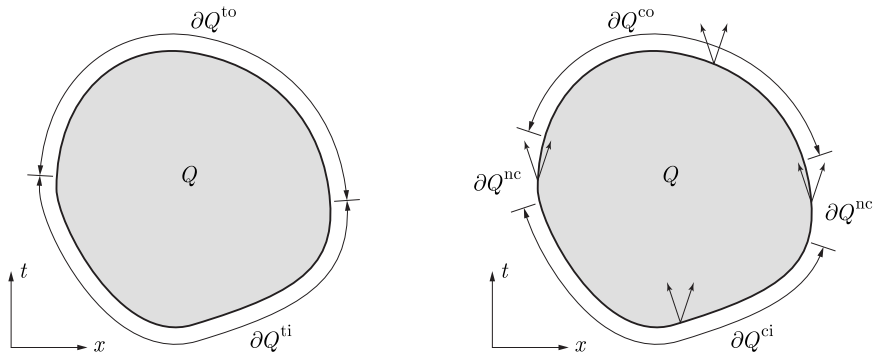

(a) Temporal partition (b) Causal partition

Figure 1. *Alternative partitions of ∂Q*

residual statement for equations [7] and [9] takes the following form. *Find* $\mathbf{u}_h \in V_h$ *such that for all* $Q \in \{Q_\alpha\}$:

$$\int_Q \dot{\mathbf{w}} \wedge (\mathbf{d}\mathbf{M}_h + \rho\mathbf{b}) + \int_{\partial Q} \left\{ \dot{\mathbf{w}} \wedge (\mathbf{M}_h^* - \mathbf{M}_h) + (\varepsilon_h^* - \varepsilon_h) \wedge \mathbf{i}\hat{\mathbf{M}} \right\} + \int_{\partial Q^{\mathrm{ti}}} \mathbf{w}_0 \wedge (\mathbf{u}_h^* - \mathbf{u}_h) \otimes \mathbf{i}\boldsymbol{\Omega} = 0 \quad \forall \mathbf{w} \in V_h^Q, \qquad [16]$$

in which a superposed '$\hat{}$' indicates a function of $\mathbf{w}$, and a subscript 'h' denotes a function of $\mathbf{u}_h$. The Stokes Theorem applied to [16] leads to the discrete weak form used in our numerical implementation:

$$\int_Q \{-\mathbf{d}\dot{\mathbf{w}} \wedge \mathbf{M}_h + \dot{\mathbf{w}} \wedge \rho\mathbf{b}\} + \int_{\partial Q} \left\{ \dot{\mathbf{w}} \wedge \mathbf{M}_h^* + (\varepsilon_h^* - \varepsilon_h) \wedge \mathbf{i}\hat{\mathbf{M}} \right\} + \int_{\partial Q^{\mathrm{ti}}} \mathbf{w}_0 \wedge (\mathbf{u}_h^* - \mathbf{u}_h) \otimes \mathbf{i}\boldsymbol{\Omega} = 0 \quad \forall \mathbf{w} \in V_h^Q. \qquad [17]$$

It is easily shown (Abedi *et al.*, 2006) that the discrete solution to [17] satisfies exactly the integral forms of Balance of Linear and Angular Momentum over every spacetime element $Q \in (Q_\alpha)$. For convenience of implementation, an alternative statement using indicial tensor notation of the weak form [17] appears in (Abedi *et al.*, 2006).

2.8. *Energy dissipation*

While the SDG formulation balances linear and angular momentum to within machine precision over every spacetime element, the method does not balance energy. Recalling [10] and [14] and enforcing the target flux values, the numerical energy dissipation for spacetime element Q is given by:

$$\varphi^{\mathrm{Q}} = \frac{1}{2}\int_{\partial Q} (\dot{\mathbf{u}}^* \wedge \mathbf{M}^* + \varepsilon^* \wedge \mathbf{i}\sigma^*) + \int_Q \dot{\mathbf{u}} \wedge \rho\mathbf{b}. \qquad [18]$$

As shown in (Abedi *et al.*, 2006), the following identity holds:

$$\varphi^{\mathrm{Q}} = \frac{1}{2}\int_{\partial Q} \{[\![\dot{\mathbf{u}}_h]\!] \cdot [\![\mathbf{M}_h]\!] + [\![\varepsilon_h]\!] \wedge [\![\mathbf{i}\mathbf{M}_h]\!]\}\,. \qquad [19]$$

The jump integrand is identically zero on ∂Q^{co} and is nonnegative on $\partial Q^{co} \cup \partial Q^{nc}$ (Petracovici, 2004). Therefore, φ^{Q} is nonnegative. The *total energy dissipation over D with respect to the target flux on ∂D*, denoted by Δ, is given by:

$$\Delta := \int_D \dot{\mathbf{u}}_h \cdot \rho\mathbf{b} + \frac{1}{2}\int_{\partial D} \{\dot{\mathbf{u}}_h^* \cdot \mathbf{M}_h^* + \varepsilon_h^* \wedge \mathbf{i}\mathbf{M}_h^*\} = \sum_{Q\in\mathcal{P}_h} \varphi^{\mathrm{Q}}. \qquad [20]$$

The total energy dissipation is clearly nonnegative, so our method is dissipative. An *a priori* error estimate reported in (Petracovici, 2004) indicates that the dissipation Δ is of order h^{2n-1}, provided that the exact solution satisfies certain regularity conditions and that all inter-element boundaries are causal. Our numerical studies suggest that the same convergence rate is achieved for arbitrary patch-wise causal partitions.

3. Adaptive implementation

In contrast to methods that use a sequence of global time steps to advance the solution in time, we implement our SDG method on unstructured spacetime meshes that admit nonuniform refinement in both space and time. We construct our spacetime meshes subject to a *causality constraint* that enables a direct, patch-by-patch, advancing-front solution procedure that interleaves mesh generation with patch-level solution procedures. This leads to an algorithm with linear computational complexity in the number of patches that is well-suited to parallel and adaptive implementation. The following subsections describe the basic SDG meshing and solution procedure and a spacetime adaptive refinement strategy that controls element-wise energy dissipation.

3.1. *Spacetime meshing and advancing-front solution procedure*

We say that a spacetime mesh is *patchwise causal* if and only if the elements in the mesh can be organized into groups of contiguous elements called *patches*, such

that the boundary of each patch consists exclusively of causal manifolds (see 2.6). Inter-element boundaries within the patch can be noncausal, so the elements within the patch must be solved simultaneously. However, the dependency graph between patches defines a partial ordering wherein the solution on each patch depends only on boundary data and solutions on earlier patches in the partial ordering. Thus, patches can be solved locally, without approximation, using only boundary data and outflow data from previously-solved patches (Abedi *et al.*, 2006). Furthermore, elements at the same level in the partial ordering are mutually independent and can be solved in parallel. This causality-based partial ordering is the basis of our advancing-front solution procedure.

We use the *Tent Pitcher* meshing procedure (Üngör *et al.*, 2002; Erickson *et al.*, 2002) to construct causal spacetime meshes in 2D $\times$ time, as illustrated in Figure 2. Tent Pitcher begins with a constant-time triangulation of the spatial domain at the initial analysis time; this is the initial *front*. A front is a triangulated spacetime surface, generally with nonuniform time coordinates. Tent Pitcher constructs a new front by advancing in time a local-minimum vertex of the current front.[2] The line segment between the old and new positions of the advancing vertex is called a *tent pole*. Each time the front advances, Tent Pitcher fills the volume between the old and new fronts with a patch (or *tent*) of tetrahedral elements that share the tent pole as a common edge. We refer to the process of erecting a new tent pole and generating the corresponding patch of elements as *pitching a tent*.

In order to guarantee that every patch is causal, we require every triangular facet in each new front to be a causal manifold. Tent Pitcher limits the height of each new tent pole to satisfy this *causality constraint*. Unfortunately, advancing the front sequentially, subject only to the causality constraint, can lead to a locking condition in which it is impossible to advance the front further. Tent Pitcher enforces a second constraint on the tent-pole height, called the *progress constraint*, to ensure that this locking condition does not occur (Erickson *et al.*, 2002). This leads to a robust, advancing-front algorithm for constructing patch-wise causal spacetime meshes.

Each new causal patch can be solved independently of all subsequent patches, using data only from the spacetime domain boundary and from adjacent, previously-solved elements. Tent Pitcher immediately passes the geometric description of each new patch, together with all required physical data, to the SDG finite element routines for solution. The required physical data include flags that describe the material type for each element, and solution fields on the adjacent, previously-solved elements. Also included are boundary data and complete descriptions of the geometry. The finite element routines compute the SDG solution on the new patch and return it to Tent Pitcher. Tent Pitcher stores the new patch solution, updates the current front to the new front, and locates a new local-minimum vertex in preparation for pitching the next tent. Thus, the processes of spacetime mesh generation and finite element solution are

2. A *local-minimum vertex* is a vertex whose time coordinate is less than or equal to the time coordinates of all its neighboring vertices.

interleaved at the patch level. Any previously-solved patch that is no longer adjacent to the updated front cannot influence subsequent solutions, so its data are written to mass storage and removed from high-speed memory. The tent-pitching cycle repeats until the entire spacetime analysis domain is covered.

This patch-wise solution method has several advantages. First, it delivers linear computational complexity in the number of patches (if the maximum degree of any vertex in the spatial triangulation is bounded). There is no need to assemble and store a global system of equations; the finite element routines are written to solve a single patch at a time. The local structure also facilitates adaptive analysis, as described in Section 3.2. If the error in the current patch is unacceptable, the mesh can be refined locally; only the solution on that particular patch need be discarded. Thus, the overall cost of the adaptive solution is reduced relative to methods that require recalculation of a global time step. Finally, the patch-by-patch solution technique lends itself to parallel computation. Multiple tents can be pitched and solved simultaneously on separate processors, subject only to the partial ordering constraint for patches. The local characteristics of the algorithm minimize interprocessor communication.

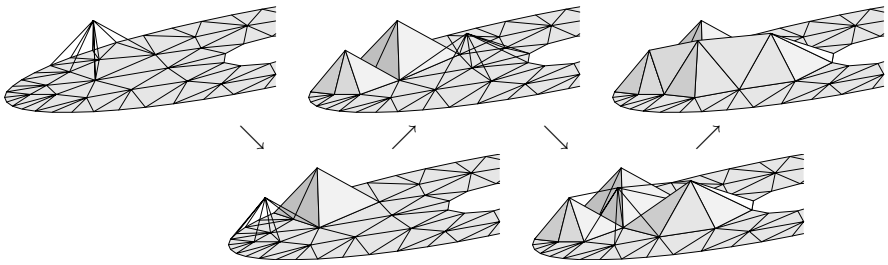

Figure 2. *Pitching tents in spacetime. Wire-frame-rendered clusters of tetrahedra indicate newly-constructed, unsolved patches; the shaded, triangulated surface depicts the current front in each image*

3.2. *Adaptive analysis*

This subsection describes adaptive extensions of the SDG method that ensure an accurate solution, especially when shocks are present. Geometric aspects of adaptive mesh refinement and coarsening are described in 3.2.1, and a dissipation-based error indicator is introduced in 3.2.2 to drive the mesh adaptation.

3.2.1. *Adaptive mesh refinement and coarsening*

We use an adaptive extension of the Tent Pitcher algorithm (Abedi *et al.*, 2004) to implement adaptive refinement and coarsening within our patch-by-patch, advancing-front solution algorithm. Rather than adapting patches of spacetime elements directly, Tent Pitcher implements adaptive refinement by managing the triangulation of the cur-

rent front. Each time a patch is solved, a local error indicator (see below) is computed for each element in the patch and tested against user-specified target values.

If the error indicator is too far above its target value in a given element, then that element is marked for *refinement* and the solver *rejects* the patch when it is returned to Tent Pitcher. Tent Pitcher, in turn, discards the rejected patch and, using a newest-vertex-bisection algorithm (see Figure 3 and (Abedi *et al.*, 2004)), refines the facets of the current front that correspond to elements marked for refinement. This effectively refines the spacetime mesh in both space and time when tent pitching is resumed, because the causality constraint dictates shorter tent-pole heights (local time steps) at vertices associated with refined facets. Note that Tent Pitcher discards the solution only on the rejected patch. The solutions on all previously-solved patches are unaffected due to the patch-wise causal structure of the spacetime grid, so the amount of redundant calculation is minimized when the front is refined.

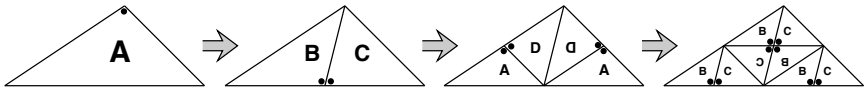

Figure 3. *Newest-vertex bisection. Tent Pitcher bisects the edge opposite the newest (marked) vertex in each triangle designated for refinement in the current front. This produces a limited set of triangle shapes, with guaranteed quality relative to the original triangle* ***A***

If the error indicator in a given element is too far below its target value, then that element is marked as *coarsenable* when it is returned to Tent Pitcher. Otherwise, if an element is neither coarsenable or marked for refinement, the element is marked as *acceptable*. Tent Pitcher accepts the solution on the current patch if all elements in the patch are either acceptable or coarsenable. In this case, Tent Pitcher stores the patch solution, advances the front, and copies the status (acceptable or coarsenable) from the patch elements to the corresponding facets of the new front.

Requests for coarsening need not be acted on immediately, since they do not involve unacceptable error. Tent Pitcher's coarsening operation involves deleting a degree-4 vertex so as to merge two pairs of adjacent, coarsenable facets into two facets in the new front. In order to maintain the integrity of the spacetime grid, each pair of facets must be coplanar before the coarsening operation can be executed. Typically, this requirement is not satisfied immediately, so Tent Pitcher postpones coarsening until it has pitched new tent poles with heights adjusted to meet the coplanarity constraint.

The adaptive refinement and coarsening operations maintain a nesting relation between the old and new fronts wherein every facet on the new front is either a subdomain of a single facet from the old front (refinement) or the union of two adjacent old facets (coarsening). The nesting property facilitates the evaluation of boundary integrals that depend on data from previously solved elements. Refinement and coarsening

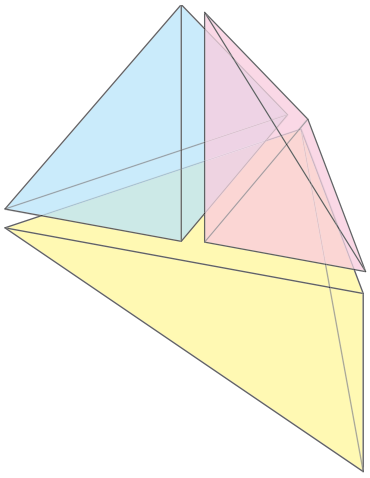

Figure 4. *Local refinement of the spacetime mesh in response to a bisection of a facet in the current front. The resulting nonconforming spacetime mesh is fully supported by the SDG formulation without projecting data from the old front to the new front. Nonconforming facets are nested to facilitate evaluation of jump terms on the element boundaries. Coarsening, the inverse of this operation, is handled in a similar fashion*

operations produce nonconforming spacetime grids, but this does not cause a problem, and there is no need to project the solution from the old front onto the new front, because the SDG formulation naturally accommodates discontinuous data. This circumvents a source of numerical error and algorithmic complexity that impacts many other adaptive algorithms while preserving exact, element-wise balance of linear and angular momentum.

3.2.2. *Adaptive control of numerical dissipation*

Although the SDG formulation balances linear and angular momentum over every spacetime element, the method is dissipative. Therefore, we must limit the numerical dissipation to obtain an accurate solution. Further, to achieve an efficient solution, we attempt to distribute the numerical dissipation evenly over the spacetime elements.

The dissipation on element Q is given by Equation [18]. Let φ^* be the target dissipation per element. The dissipation on element Q is considered acceptable when $\underline{\varphi} \leq \varphi^{\mathrm{Q}} \leq \overline{\varphi}$, where $\underline{\varphi} = (1-\eta)\varphi^*$ and $\overline{\varphi} = (1+\eta)\varphi^*$ in which η is a user-specified parameter subject to $0 < \eta < 1$. Refinement is required when $\varphi^{\mathrm{Q}} > \overline{\varphi}$, and element Q is coarsenable when $\varphi^{\mathrm{Q}} < \underline{\varphi}$. The parameter η must be chosen sufficiently large to minimize undesirable cycling between coarsening and refinement. We use $\eta = 0.2$ in our current implementation.

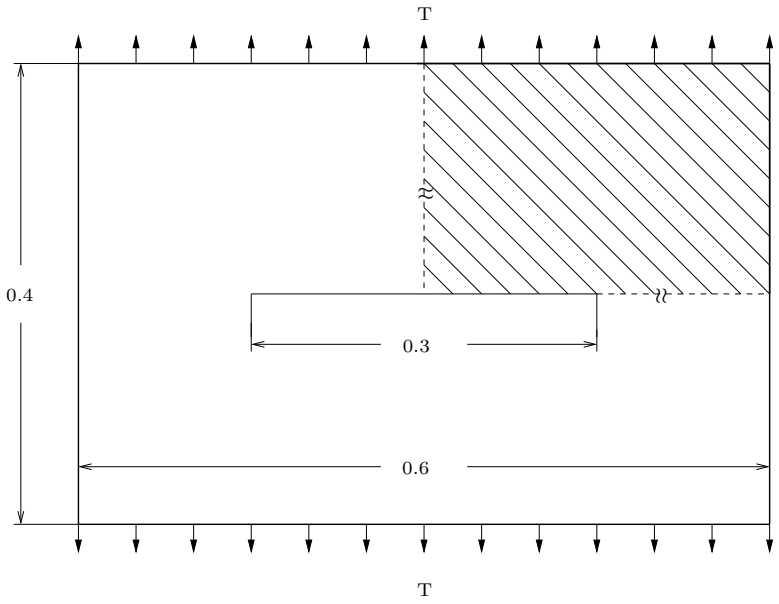

Figure 5. *Spatial domain and boundary conditions for the crack scattering problem*

4. Numerical example

This section presents numerical solutions of a crack-tip wave-scattering problem that demonstrate the performance of our adaptive algorithm. Crack-tip singularities and complex patterns of scattered shock fronts produce a challenging, multi-scale analysis problem.

Figure 5 shows a center-cracked plate that we model using plane-stress assumptions, Young's modulus $E = 10$, Poisson ratio $\nu = 0.3$, and density $\rho = 2$. A spatially uniform tensile traction of magnitude T acts along the top and bottom edges of the plate. The magnitude T vanishes at negative times, ramps from zero at time $t = 0.0$ to a maximum value of 10 at time $t = 0.002$, and holds constant at the maximum value until the simulation interval terminates at time $t = 0.150$. The ramping approximates a stress-velocity shock while maintaining continuity of the loading. We apply symmetry boundary conditions to model only the shaded region shown in the figure, and we use complete cubic polynomials to model the displacement field within each spacetime tetrahedron. A uniform 2×4 rectangular grid defines the initial space mesh, with each rectangle subdivided into two triangles.

Figure 6 shows the influence of the target dissipation φ^* on the accuracy and cost of the solution. We use the total numerical dissipation Δ, normalized by the *total inflow energy* $\mathbf{E}_0$, to measure the solution error and the total number of elements

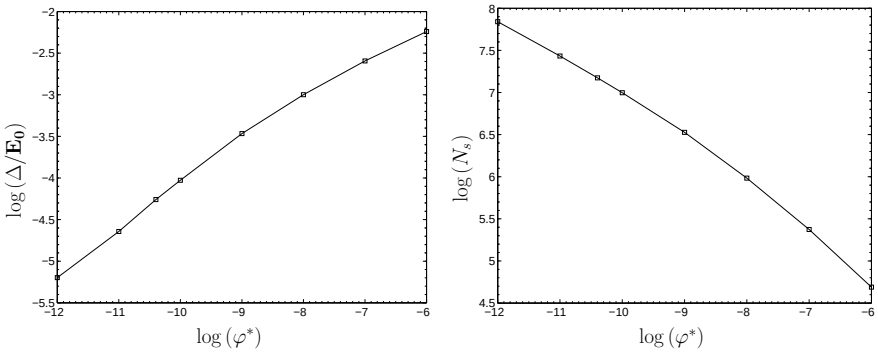

(a) Total energy dissipation Δ versus target per-element dissipation φ^*

(b) Number of elements solved N_s versus target per-element dissipation φ^*

Figure 6. *Influence of target per-element dissipation on solution accuracy and cost*

solved N_s to indicate the cost of the solution.[3] Figure 6(a) shows that the energy dissipation converges toward zero as φ^* approaches zero. We observe in Figure 6(b) that the cost N_s increases monotonically as φ^* decreases.

Figure 7 compares the efficiency of the h-adaptive and nonadaptive versions of the SDG method. The results for the nonadaptive case were obtained using static, uniform refinements of the initial mesh. The adaptive algorithm is more efficient throughout the range of this study, as it delivers less dissipation for any given value of N_s. Furthermore, the adaptive convergence rate increases monotonically with increasing N_s, while there is no clear trend for the nonadaptive case.

Figure 8 shows the state of the spacetime mesh constructed by the adaptive Tent Pitcher algorithm at an intermediate stage of the simulation. The spatial directions are aligned with the horizontal axes, and time increases upward in the vertical direction. The fine details of the elastodynamic solution are clearly evident in the pattern of mesh refinement. The dark diagonal bands along the right face of the spacetime volume are traces of plane waves generated by the sudden traction loading, while the lighter diagonal band ascending at a steeper angle traces the trajectory of a Rayleigh wave moving along the free edge of the plate.

The spacetime trajectory of the crack tip runs along the vertical center-line of the left face of the spacetime volume. The apex of the cone-shaped region of mesh refinement indicates the initial scattering event. The separation of the scattered wave into dilatational and shear components can be seen in the pattern of refinement. The outer perimeter of the cone indicates the progress of the faster-moving dilatational wave, while the dark circular band within the cone traces the trajectory of the slower

3. The count N_s includes elements in patches that are ultimately rejected due to unacceptable error since solving these elements still contributes to the total cost of the solution.

shear wave. Figure 8(b) shows a detail of the spacetime mesh in the vicinity of the initial scattering event. The diagonal band of intense refinement traces a Rayleigh wave moving along the free surface of the crack, while the vertical band shows steady refinement that captures singular fields at the stationary crack tip. Regions of milder refinement indicate the extent of the dilatational wave.

Instances of nonconforming spacetime elements, associated with both refinement and coarsening operations, can be found at various locations in the mesh. These nonconforming features facilitate the construction of strongly graded meshes and do not require special treatment in the SDG formulation. In this example, the ratio of the largest to smallest element diameter is 1024. The ability of the adaptive SDG method to limit refinement to the trajectories of moving shocks and the avoidance of a global time step lead to significant computational savings.

Figure 9 shows a time sequence of visualizations of the adaptive solution; the images were generated by a pixel-exact visualization system developed by Garland *et al.* (Zhou *et al.*, 2004). The strain energy density field is mapped to color, with blue indicating zero energy density and red and violet indicating the highest values. The magnitude of the velocity vector is mapped to the height field, which is then shaded by a lighting model to reveal its form. The visualization clearly reveals fine features of the solution such as Rayleigh waves moving back and forth along the crack surface and the scattered shear and pressure waves emanating from the crack-tip (see Figures 9(c)-9(h)). For purposes of comparison between the spacetime mesh and the solution, we note that the top of the spacetime volume in Figure 8(a) is at roughly the same time as the instantaneous solution depicted in Figure 9(c).

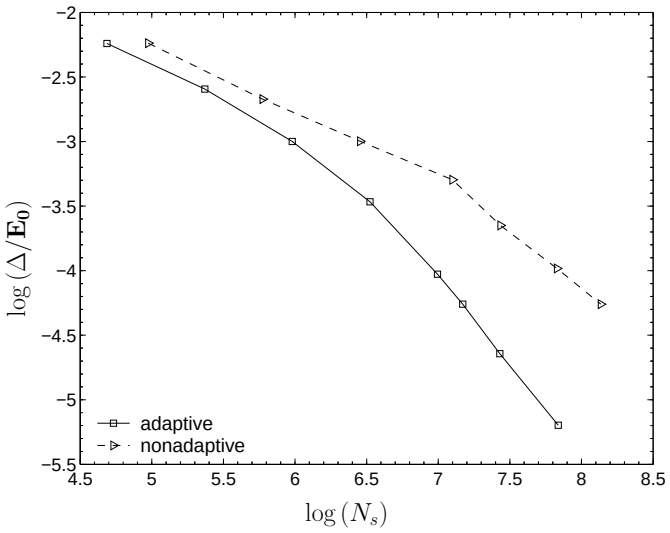

Figure 7. *Energy dissipation Δ versus number of elements solved N_s*

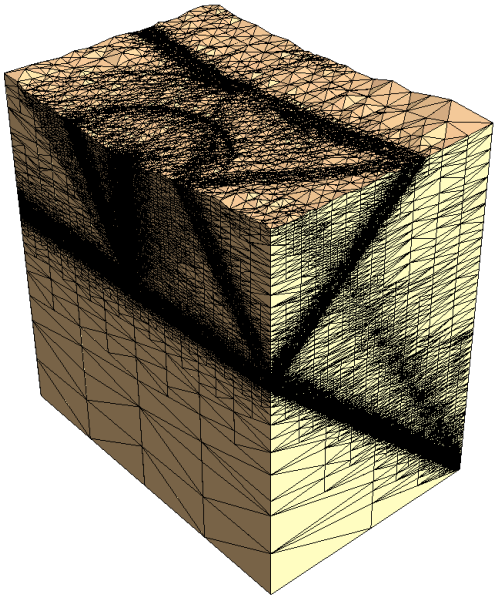

(a) Partial mesh with 11 million tetrahedra

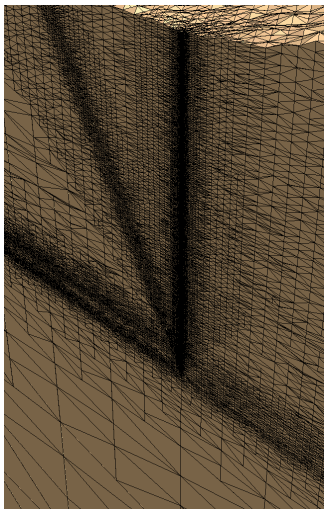

(b) Detail of the initial crack-tip scattering event

Figure 8. *Adaptive space-time mesh for the crack-tip wave scattering problem*

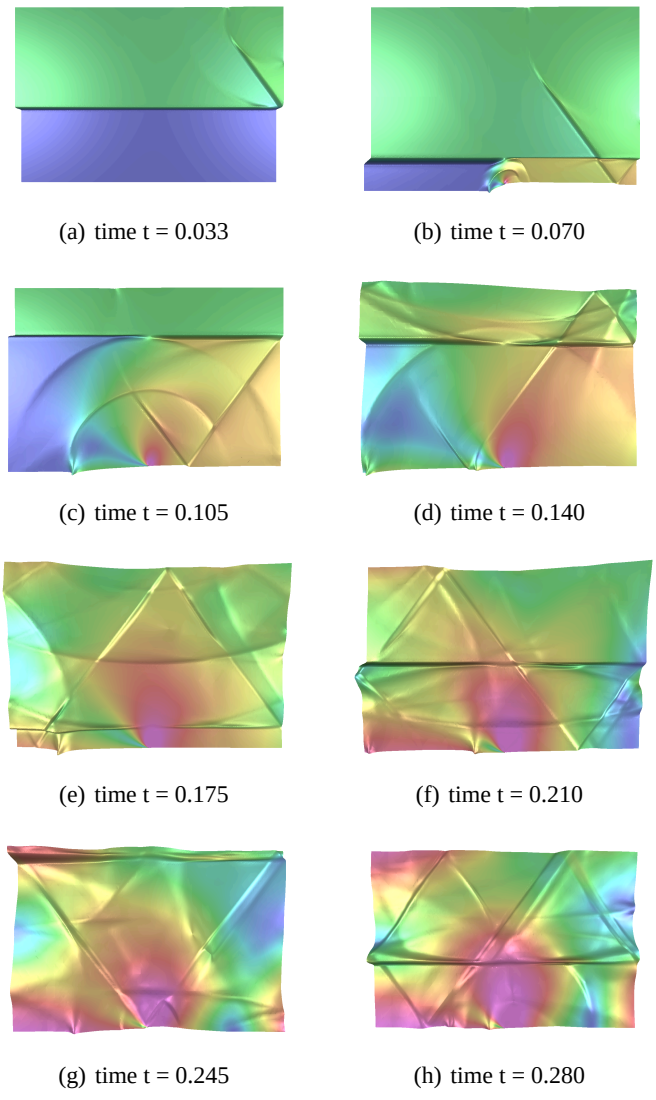

(a) time t = 0.033 (b) time t = 0.070

(c) time t = 0.105 (d) time t = 0.140

(e) time t = 0.175 (f) time t = 0.210

(g) time t = 0.245 (h) time t = 0.280

Figure 9. *Elastic wave scattering by a stationary crack-tip (at center of lower edge)*

Small-scale features, such as the shock fronts, are well resolved. The solution is free of spurious oscillations, although no extra stabilization has been added to the SDG formulation. A small amount of overshoot in the derivative fields can be observed in the vicinity of shock fronts, but the overshoot reduces with adaptive refinement and the shocks leave no artifacts in their wakes.

5. Conclusions

We have presented an h-adaptive implementation of the spacetime-discontinuous Galerkin method for linearized elastodynamics. Our method is unconditionally stable, and it balances linear and angular momentum with respect to Godunov boundary values on every spacetime element. However, it is mildly dissipitive, so our adaptive scheme is designed to limit the numerical energy loss. The method requires no extra stabilization to deliver oscillation-free solutions at shocks. Patch-wise causal spacetime grids support a patch-by-patch solution procedure with linear complexity in the number of patches and a patch-level adaptive refinement strategy. Refinement operations only affect the current patch, so the need for redundant calculations during adaptive refinement is minimized. Coarsening does not reduce the method's accuracy or interfere with its balance properties because there is no need to project the solution from the old front onto the new front. The SDG method admits nonconforming grids, and we use this feature to construct strongly graded grids as required in multi-scale problems. Our use of unstructured spacetime grids, adapted simultaneously in space and time, delivers high-resolution simulations of shocks and other transient phenomena at a reasonable cost.

Several potential enhancements and extensions of our adaptive method are worthy of mention. We are investigating a broader vocabulary of adaptive mesh operations to transform the active front in Tent Pitcher. These include edge flips, edge deletion and insertion as well as inclined tent poles. The additional operations could be used to improve the geometric quality of the spacetime mesh, to refine and coarsen more efficiently and to support front-tracking models for problems with moving interfaces. Improving the geometric quality of the mesh is especially important because our *a priori* error estimate depends on a lower bound for the worst element quality in the mesh. Moreover, numerical studies show that low-quality elements with extreme aspect ratios can lead to ill-conditioning in the patch-wise SDG equations.[4] The use of inclined tent poles is the spacetime equivalent of an r-adaptive procedure. This capability could be used to optimize element quality, to track moving interfaces or to model crack propagation.

4. The quality of the initial space mesh is an important factor in determining the quality of the spacetime mesh in our current implementation. Even with the addition of the active quality control measures proposed here, the initial space mesh would still affect the quality of the early spacetime mesh, so procedures for improving the quality of the initial space mesh might be needed in some cases.

In addition to nonconforming meshes, the SDG formulation accommodates jumps in polynomial order between adjacent elements. Thus, it provides a natural platform for implementing hp-adaptive analysis procedures. The objective would be to use h-refinement and low-order polynomials in the vicinity of shocks and other solution features with limited regularity and to use elements with higher-order polynomials in regions where the solution is smooth. Reductions in the convergence rate in regions with low regularity can be used to detect the locus of shocks, as described in (Krivodonova *et al.*, 2004).

The integration and assembly of the patch equations account for a relatively large percentage of our computational load. The cost of equation solving is smaller than in conventional algorithms because the patch-level systems are relatively modest in size. Our current implementation uses Gaussian quadrature to evaluate the element integrals. Substantial speed-ups could be realized either by using analytical quadrature formulas for simplices or by eliminating redundant calculations as in the *quadrature-free methods* (Atkins *et al.*, 1998). We are also working on a parallel version of the adaptive algorithm. Our advancing-front solution algorithm has a natural parallel structure; patches can be pitched and solved simultaneously with very little interprocessor communication. The main challenge in the parallel implementation is to maintain load balance between processors as the adaptive procedure modifies the local density of the mesh.

Acknowledgements

The authors gratefully acknowledge the contributions of Shuo-Heng Chung, Yong Fan, Michael Garland, and Yuan Zhou to this work. Support from the Center for Process Simulation and Design (CPSD) is gratefully acknowledged. The U.S. National Science Foundation supports research in CPSD *via* grant NSF DMR 01-21695.

6. References

Abedi R., Chung S. H., Erickson J., Fan Y., Garland M., Guoy D., Haber R. B., Sullivan J., Zhou Y., " Space-time meshing with adaptive refinement and coarsening", *Proceedings 20th Annual ACM Symposium on Computational Geometry*, Brooklyn, NY, June, 2004, p. 300-309.

Abedi R., Haber R. B., Petracovici B., " A Spacetime Discontinuous Galerkin Method for Elastodynamics with Element-level Balance of Linear Momentum", *Computer Methods in Applied Mechanics and Engineering*, vol. 195, n° 25-28, 2006, p. 3247-3273.

Atkins H. L., Shu C. W., " Quadrature-Free Implementation of Discontinuous Galerkin Method for Hyperbolic Equations", *AIAA Journal*, vol. 36, 1998, p. 775-782.

Bajer C. I., " Adaptive mesh in dynamic problems by the space-time approach", *Computers and Structures*, vol. 33, n° 2, 1989, p. 319-325.

Bajer C. I., Bogacz R., Bonthoux C., " Adaptive space-time elements in the dynamic elastic-viscoplastic problem", *Computers and Structures*, vol. 39, n° 5, 1991, p. 415-423.

Becache E., Joly P., Rodriguez J., " Space-time mesh refinement for elastodynamics. Numerical results", *Computer Methods in Applied Mechanics and Engineering*, vol. 194, n° 2-5 SPEC ISS, 2005, p. 355-366.

Bishop R. L., Goldberg S. I., *Tensor Analysis on Manifolds*, Prentice Hall, Englewood Cliffs, New Jersey, 1980. Reprinted By Dover (1980).

Cho J.-W., Youn S.-K., " A Hierarchical time adaptive refinement scheme for the finite element elastodynamics", *Computers and Structures*, vol. 56, n° 4, 1995, p. 645-650.

Costanzo F., Huang H., " Proof of unconditional stability for a single-field discontinuous Galerkin finite element formulation for linear elasto-dynamics", *Computer Methods in Applied Mechanics and Engineering*, vol. 194, 2005, p. 2059-2076.

Erickson J., Guoy D., Sullivan J., Üngör A., " Building spacetime meshes over arbitrary spatial domains", *Proceedings of the 11th International Meshing Roundtable*, Sandia National Laboratories, 2002, p. 391-402.

Fleming W. H., *Functions of Several Variables*, Addison-Wesley, Reading, Massachusetts, 1964.

French D. A., " A space-time finite element method for the wave equation", *Computer Methods in Applied Mechanics and Engineering*, vol. 107, 1993, p. 145-157.

Guo B., Babuška I., " The h-p version of finite element method, Part I: The basic approximation results", *Computational Mechanics*, vol. 1, n° 1, 1986a, p. 21-41.

Guo B., Babuška I., " The h-p version of finite element method, Part II: General results and applications", *Computational Mechanics*, vol. 1, n° 3, 1986b, p. 203-220.

Han B., Zhou X., Liu J., " Adaptive multigrid method for numerical solutions of elastic wave equation", *Applied Mathematics and Computation , New York*, vol. 133, 2002, p. 609-614.

Hughes T. J. R., Hulbert G. M., " Space-time finite element methods for elastodynamics: Formulations and error estimates", *Computer Methods in Applied Mechanics and Engineering*, vol. 66, 1988, p. 339-363.

Hulbert G. M., Hughes T. R. J., " Space-time finite element methods for second order hyperbolic equations", *Computer Methods in Applied Mechanics and Engineering*, vol. 84, 1990, p. 327-348.

Johnson C., " Discontinuous Galerkin finite element methods for the wave equation", *Computer Methods in Applied Mechanics and Engineering*, vol. 107, 1993, p. 117-129.

Joo K.-J., Wilson E. L., " An adaptive finite element technique for structural dynamic analysis", *Computer and Structures*, vol. 30, n° 2, 1988, p. 1319-1339.

Krivodonova L., Xin J., Remacle J. F., Chevaugeon N., Flaherty J. E., " Shock detection and limiting with discontinuous Galerkin methods for hyperbolic conservation laws", *Applied Numerical Mathematics*, vol. 48, 2004, p. 323-338.

Lesaint P., Raviart P. A., " On a finite element method for solving the neutron transport equation", *in* de Boor (ed.), *Mathematical aspects of fintie elements in partial differential equations*, Academic Press, New York, p. 89-123, 1974.

Mackerle J., " Error estimates and adaptive finite element methods: A bibliography (1990-2000)", *Engineering Computations*, vol. 18, n° 5/6, 2001, p. 802-914.

Petracovici B., Analysis of a Spacetime Discontinuous Galerkin Method for Elastodynamics, PhD thesis, Department of Mathematics, University of Illinois, 2004.

Reed W. H., Hill T. R., Triangular mesh methods for the neutron transport equation , Technical report, Los Alamos Scientific Laboratory, Los Alamos, 1973.

Richter G. R., " An explicit finite element method for the wave equation", *Applied Numerical Mathematics*, vol. 16, 1994, p. 65-80.

Safjan A., Oden J. T., " High-order Taylor-Galerkin and adaptive h-p methods for second-order hyperbolic systems: Application to elastodynamics", *Computer Methods in Applied Mechanics and Engineering*, vol. 103, 1993, p. 187-230.

Spivak M., *Calculus on Manifolds*, W. A. Benjamin, New York, 1965.

Üngör A., Sheffer A., " Pitching tents in space-time: Mesh generation for discontinuous Galerkin method", *International Journal of Foundations of Computer Science*, vol. 13, n° 2, 2002, p. 201-221.

Wiberg N.-E., Zeng L., Li X., " Error estimation and adaptivity in elastodynamics", *Computer Methods in Applied Mechanics and Engineering*, vol. 101, 1992, p. 369-395.

Yin L., A New Spacetime Discontinuous Galerkin Finite Element Method for Elastodynamics Analysis, PhD thesis, Department of Theoretical & Applied Mechanics, University of Illinois, 2002.

Yin L., Acharia A., Sobh N., Haber R. B., Tortorelli D. A., " A Spacetime discontinuous Galerkin method for elastodynamics analysis", *Discontinuous Galerkin Methods: Theory, Computation and Applications, B. Cockburn and G. Karriadakis and C. W. Shu(eds)*, Springer Verlag, 2000, p. 459-464.

Zhou Y., Garland M., Haber R. B., " Pixel-Exact Rendering of Spacetime Finite Element Solutions", *Proceedings of IEEE Visualization 2004*, October, 2004, p. 425-432.